

Synthesis of Hierarchical Porous Zn-Doped SnO₂ Spheres and Their Photocatalytic Properties

Jing Wang, Huiqing Fan, and Huawa Yu

(Submitted July 18, 2015; in revised form September 10, 2015; published online October 23, 2015)

The undoped and Zn-doped SnO₂ products have been synthesized by a solvothermal method. With the Zn doping concentration changing from 0 to 20 mol%, the SnO₂ morphology evolved from aggregated nanoprisms into hierarchical porous spheres. The products were characterized by x-ray diffraction, Raman spectroscopy, field emission scanning electron microscopy, energy-dispersive spectroscopy, transmission electron microscopy, selected area electron diffraction, UV-Vis absorption spectra, and photoluminescence spectra analysis. The results showed that Zn doping concentration significantly influenced on the microstructure, size, morphology, and optical property of the SnO₂ products. Furthermore, the influence of the doping effect on the photocatalytic performance of the as-prepared SnO₂ products was compared. The results revealed that 20 mol% Zn-doped SnO₂ with hierarchical porous spheres exhibited excellent efficiency of photocatalytic activity, which could be attributed to their abundant oxygen vacancies, large specific surface area, and porous structure.

Keywords doping, microstructure, photocatalytic, SnO₂

1. Introduction

Various organic compounds such as dyes from textile and other industries contaminate water and pose a threat to ecosystem. Numerous efforts have been devoted for the removal of dye from industrial wastewater. In particular, photocatalytic degradation of organic pollutants using nanostructured semiconductors offers great potential for the complete elimination of toxic chemicals (Ref 1, 2). Photocatalysis is based on the light absorption of semiconductors to excite the electrons from valence band to conduction band and create electron-hole pairs, which help in the degradation of organic pollutants (Ref 3). Up to now, many semiconductor photocatalysts have been attempted for the photocatalytic degradation of environmental pollutants. Among those semiconductors, tin oxide (SnO₂), which is an n-type semiconductor with a wide band gap ($E_g = 3.6$ eV), has been broadly studied as a photocatalyst due to its chemical stability, a suitable band gap, nontoxicity, low cost, and photoactivity (Ref 4-6). However, enhancing the photocatalytic efficiency of SnO₂ to meet the practical application requirements is still a challenge because of the bottleneck of poor quantum yield caused by the rapid recombination of photogenerated electrons and holes (Ref 7, 8). It is well known that an appropriate amount of transition metal ions doped into SnO₂ can introduce electron capture

centers and may as well change the crystallinity of SnO₂, resulting in the production of some defects and thereby a decrease in electron/hole recombination centers. Thus, doping by metal ions is recognized as an effective modification method to improve the reactivity of light-responsive SnO₂ (Ref 9).

The photocatalytic performance of the material is also dependent on its structure and morphology. The SnO₂ nanomaterials with various dimensions have been widely studied in photocatalysts, such as nanoparticles (Ref 10), nanorods (Ref 11), nanosheets (Ref 12), and hierarchical architectures (Ref 13). Compared with low-dimensional structures, hierarchical structures possess large specific surface area and better inherent properties, such as more efficient light harvesting, high organic dye or pollutant adsorption, and unique hierarchical characteristics (Ref 14, 15). Thus, for use as a practical photocatalyst, hierarchical SnO₂ nanomaterials assembled by nanoparticles with enhanced photocatalytic properties are highly desirable. In our study, Zn-doped SnO₂ with hierarchically porous architectures was prepared by a simple one-step hydrothermal method. The effects of the Zn dopants on the structures and optical properties of the SnO₂ were discussed in detail. Furthermore, the efficiency of the doping effect on the photocatalytic performance of synthesized SnO₂ products was compared.

2. Experimental Section

2.1 Photocatalyst Preparation

All chemicals used herein were of analytic grade without further purification. In a typical synthesis, 2 mmol of SnCl₄ was dissolved in 30 mL of a water/ethanol mixture (1:1, v/v) to get a solution A. 0.1 mmol NaOH and a series of different moles (0-0.4 mmol, corresponding to 0-20% molar weight of tin ions) of Zn(CH₃COO)₂·2H₂O were dissolved in 10 mL water to get a solution B. Then under the ceaseless stir, the solution B was slowly added to solution A. After several minutes of stirring, the reaction mixture was transferred into a 50-mL Teflon vessel and finally sealed in a hydrothermal autoclave. The autoclave was

Jing Wang, State Key Laboratory of Solidification Processing, School of Materials Science and Engineering, Northwestern Polytechnical University, Xi'an 710072, China; and School of Science, Xi'an Polytechnic University, Xi'an 710048, China; **Huiqing Fan**, State Key Laboratory of Solidification Processing, School of Materials Science and Engineering, Northwestern Polytechnical University, Xi'an 710072, China; and **Huawa Yu**, School of Science, Xi'an Polytechnic University, Xi'an 710048, China. Contact e-mails: wangjing_oct@126.com and hqfan3@163.com.

heated to 190 °C for 18 h and allowed to cool down to ambient temperature naturally. The resulting powder was separated by centrifugation and washed several times with water and ethanol. Finally, the powder was dried at 60 °C for 24 h.

2.2 Characterizations

X-ray diffraction (XRD) patterns were obtained on a SmartLab x-ray diffractometer with Cu-K α radiation ($\lambda = 1.5406 \text{ \AA}$). The morphologies of the products were examined using a Zeiss Supra 55 field emission scanning electron microscopy (FE-SEM) operated at 15 kV. Transmission electron microscopy (TEM, JEM-3010, Questar, New Hope, USA) was performed using an acceleration voltage of 300 kV. The Raman spectra (inVia, Renishaw, Gloucestershire, UK) were excited by a 532 nm Nd:YAG laser at room temperature. The photoluminescence (PL) spectra were recorded at room temperature with an excitation wavelength of 300 nm by a fluorescence spectrophotometer (HORIBA fluoromax-4). The ultraviolet-visible (UV-Vis) absorption spectra were recorded by spectrophotometer (PerkinElmer, Lambda 950).

2.3 Photocatalytic Activity Test

The photocatalytic performance of the as-prepared samples was evaluated by photocatalytic degradation of RhB under UV light irradiation. 0.1 g samples were dispersed in the 100 mL RhB aqueous solution (10 mg/L). The mixed suspensions were magnetically stirred for 30 min in the dark to reach an adsorption-desorption equilibrium. Then, the suspension was irradiated by UV light (300 W mercury lamp) under continuous magnetic stirring. Every 15 min of irradiation time, a 5-mL aliquot of the reaction mixture was centrifuged and characterized using an UV-Vis spectrophotometer, and the total reaction time was 60 min.

3. Results and Discussion

The XRD patterns of the resulting products are shown in Fig. 1. The analysis of the diffraction peaks revealed the presence of rutile-type tetragonal structure phase (JCPDS Card No: 71-0652) in all the compositions. No extra peaks of impurity phase were observed in the patterns which indicate that the powders obtained in the present work are single-phase SnO₂ nanoparticles. As the doping concentration increases, the intensity of XRD peaks decreases and full width at half maximum (FWHM) increases, which is due to the degradation of crystallinity. This means that even though the Zn²⁺ ions occupy the regular lattice site of Sn⁴⁺, it produces crystal defects around the dopants and the charge imbalance arising from this defect changes the stoichiometry of the materials. The lattice parameters for undoped SnO₂ and Zn-doped SnO₂ nanoparticles were estimated from the equation:

$$\frac{1}{d_{hkl}^2} = \frac{h^2 + k^2}{a^2} + \frac{l^2}{c^2}, \quad (\text{Eq 1})$$

where a and c are the lattice parameters, h , k , and l are the Miller indices, and d_{hkl} is the interplanar spacing for the plane (hkl). This interplanar spacing can be calculated from

$$2d_{hkl}\sin\theta = n\lambda, \quad (\text{Eq 2})$$

where λ is the wavelength of x-ray, θ is the Bragg diffraction angle, and n is the order diffraction ($n = 1$). As shown in

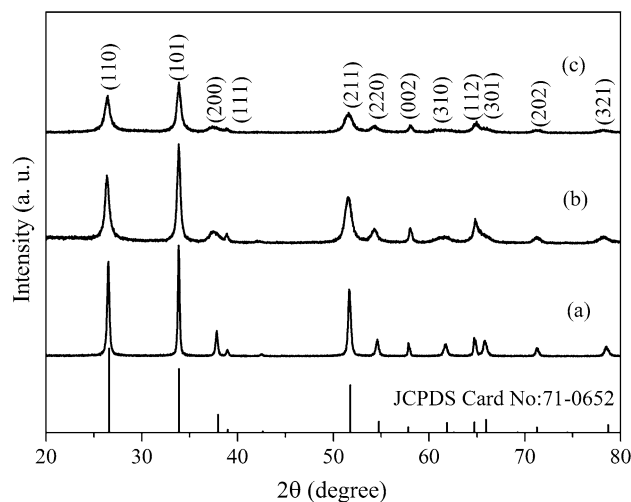


Fig. 1 XRD patterns of the as-prepared products: (a) undoped SnO₂, (b) 10 mol% Zn-doped SnO₂, and (c) 20 mol% Zn-doped SnO₂

Table 1 Lattice parameters and grain sizes of pure SnO₂ and Zn-doped SnO₂

Sample	a , nm	c , nm	Grain size, nm
Pure SnO ₂	4.752	3.1858	37.6
[Zn ²⁺]/[Sn ⁴⁺] = 0.1	4.798	3.1767	21.4
[Zn ²⁺]/[Sn ⁴⁺] = 0.2	4.808	3.1718	18.5

Table 1, the calculated values of lattice parameters exhibit an increase along a direction and a decrease along c direction. The ionic radius of Sn⁴⁺ is 0.71 Å, which is small compared to 0.74 Å for Zn²⁺ (Ref 16). Due to this fact, the lattice distortion may be ascribed to Zn²⁺ replacing Sn⁴⁺ in lattice. Furthermore, the average crystallite sizes can be obtained using Scherrer's formula $D = K\lambda/\beta\cos\theta$ (Ref 17), where D is the average crystallite size, β is the FWHM in radians, λ is the x-ray wavelength (Cu-K $\alpha = 0.154 \text{ nm}$), θ is the Bragg diffraction angle, and K is a correction factor which is taken as 0.9. As shown in Table 1, the calculated grain size decreased from 38 nm to 19 nm with the increase of Zn doping concentration.

In order to confirm the substitution of Sn⁴⁺ by Zn²⁺ ions, Raman spectroscopy measurements have also been performed. It is well known that SnO₂ has a tetragonal structure having two tin atoms and four oxygen atoms per unit cell with a space group D_{4h}¹⁴ (P4₂/mm). Six unit cell atoms give a total of 18 vibrational modes in the first Brillouin zone. Among these modes, A_{1g}, E_g, B_{1g}, and B_{2g} modes are Raman active (Ref 18, 19). Figure 2 shows the room-temperature Raman spectra of undoped and Zn-doped SnO₂. The most intense Raman peak at 619 cm⁻¹ can be attributed to the A_{1g} mode. The Raman bands at 495 and 761 cm⁻¹ are the vibration modes E_g and B_{2g}, respectively. The A_{1g} and B_{2g} modes are nondegenerate and vibrate in the plane perpendicular to the c -axis, whereas the doubly degenerated E_g mode vibrates in the direction of the c -axis (Ref 20). These peaks further confirm that the as-prepared products possess the characteristics of the tetragonal rutile structure. Apart from this, one more peak is observed at around

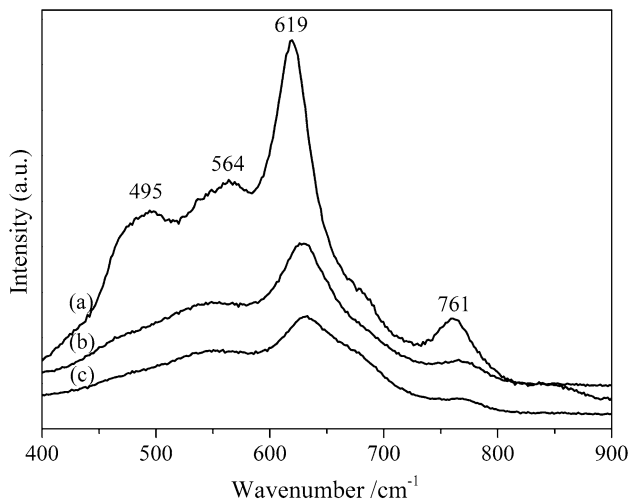


Fig. 2 Raman spectra of the as-prepared products: (a) undoped SnO₂, (b) 10 mol% Zn-doped SnO₂, and (c) 20 mol% Zn-doped SnO₂

564 cm⁻¹. This extra peak can be attributed to oxygen vacancies and defects, so there may be a possibility of the appearance of new modes in Raman spectra (Ref 21). It is interesting to note that the A_{1g} and B_{2g} modes shift toward higher wavenumber (blueshift) with the increase in Zn doping concentration, indicating that microstructural transformations occurred which is related to the effect of the incorporated Zn atoms. In addition, the Zn doping induces a broadening and an intensity reduction in all the Raman peaks. Particularly, the E_g mode (at 495 cm⁻¹) is much influenced by the Zn doping and vanished more quickly. The broadening and reduction of the Raman peaks are not only related to phonon confinement effect caused by decreasing crystallite size, but also connected with the defects and vacancy clusters in SnO₂ crystals (Ref 22-24). As the E_g mode is the result of two oxygen atoms vibrating parallel to the c-axis, but in opposite directions, it is more sensitive to oxygen vacancies than other modes (Ref 25). Therefore, the sharp decrease of E_g peak may be related to the oxygen vacancies in Zn-doped SnO₂ crystals.

Typical SEM images of undoped and Zn-doped SnO₂ nanoparticles are presented in Fig. 3(a)-(d). Without Zn doping, the SnO₂ exhibits aggregation of nanoprisms with large size as shown in Fig. 3(a). These SnO₂ nanoprism units possess a square end face with lengths ranging from 600 to 800 nm and diameters of 160-190 nm. Figure 3(b) shows the 10 mol% Zn-doped SnO₂, which comprised needle-like nanorods with smaller lengths of 300-400 nm and smaller diameters of 50-60 nm in contrast to the case without doping. When the Zn doping concentration was increased to 20 mol%, the hierarchical porous spheres were formed, as shown in Fig. 3(c)-(d). In a high-magnification SEM image (Fig. 3c), it can be seen that the surface of hierarchical architecture is made up of interconnected SnO₂ nanorods leaving behind a porous network. The length and diameter of these nanorods were approximately 30 and 300 nm, respectively. In a low-magnification SEM image (Fig. 3d), some breakage of the microspheres reveals that the inner part of hierarchical structures is also composed of loosely packed nanorods and appeared to be highly porous. Based on the observation above, it could be concluded that incorporation of Zn doping strongly modified the morphology, size, and

aspect ratio (length/diameter) of SnO₂ structure. The surface energies of SnO₂ facets follow the trend (110) < (100) < (101) < (001), assuming the preferential growth direction along the c-axis. However, according to Leite's research (Ref 26), the surface energy between the different crystal faces is close. For example, the surface energy of the (001) surface is 1.53 times greater than that of the (110) surface, while the (101) surface presents a surface energy of only 1.19 times that of the (110) surface. This implies that it is difficult to obtain low-dimensional SnO₂ nanocrystals with high aspect ratio. The Zn incorporated in the crystal lattice induces large lattice distortion and defects occurred in the pristine structure, which may modify the surface energy of some crystallographic planes and thus increase the aspect ratio (length/diameter) of SnO₂ structure. Moreover, the surface composition of Zn-doped SnO₂ was determined by FE-SEM-based energy-dispersive spectroscopy (EDS) analysis as shown in Fig. 3(e)-(f). The products are composed of only Sn, O, and Zn elements and the atomic ratios of Zn/Sn are 15% and 29%, respectively. In order to obtain further information about the hierarchical architecture of 20 mol% Zn-doped SnO₂, TEM and HRTEM analyses were performed. The typical TEM image (Fig. 3g) shows that the surface of hierarchical architecture is constructed with nanorods, which is consistent with the SEM results. The HRTEM image (Fig. 3h) provides further insight into the structure of individual nanorods. The lattice plane with an interplanar distance of 0.34 nm is measured, corresponding to the (110) planes of the SnO₂ rutile structures. The SAED (inset of Fig. 3h) rings are relatively sharp and can be assigned to polycrystalline SnO₂.

The optical absorption spectra of the as-prepared products are shown in Fig. 4. The intense peaks of the 20 mol% Zn-doped SnO₂ is higher than those of undoped and 10 mol% Zn-doped SnO₂. Combined with SEM analyses, the nanorods of hierarchical porous spheres possess high aspect ratio and smallest size, which contribute to improving their specific surface area and consequently enabling higher light harvesting. Additionally, the porous structure of the 20 mol% Zn-doped SnO₂ allows multiple reflections of UV light, which leads to larger UV light adsorption capacity (Ref 27). Moreover, the Tauc relation was used to calculate the direct band gap (Ref 28):

$$\alpha h\nu = A(h\nu - E_{\text{gap}})^{1/2},$$

where α is the absorption coefficient, h is the Planck's constant, ν is the frequency of the incident photon, E_{gap} is the optical band gap, and A is constant. The optical band gap for the absorption peak can be obtained by extrapolating the linear portion of $(\alpha h\nu)^2$ versus $h\nu$ curve as presented in the inset of Fig. 4. The band gap value is determined by extrapolating the linear portion of the plot to energy axis. The measured band gaps were found to be 3.52, 3.40, and 3.34 eV for undoped and 10 and 20 mol% Zn-doped SnO₂, respectively. The band gap values of the Zn-doped SnO₂ are lower than that of the undoped SnO₂, which indicates that the introduction of Zn atoms modified the electronic structures of the pristine SnO₂.

Figure 5 shows the PL emission spectra of the as-prepared products. PL spectra of all the nanoparticles show almost identical peak positions for the entire wavelength range. Several visible emission bands are observed in the PL spectra, which include a broad asymmetric band centered at approximately 467 nm and a weak emission at 561 nm. In addition, the

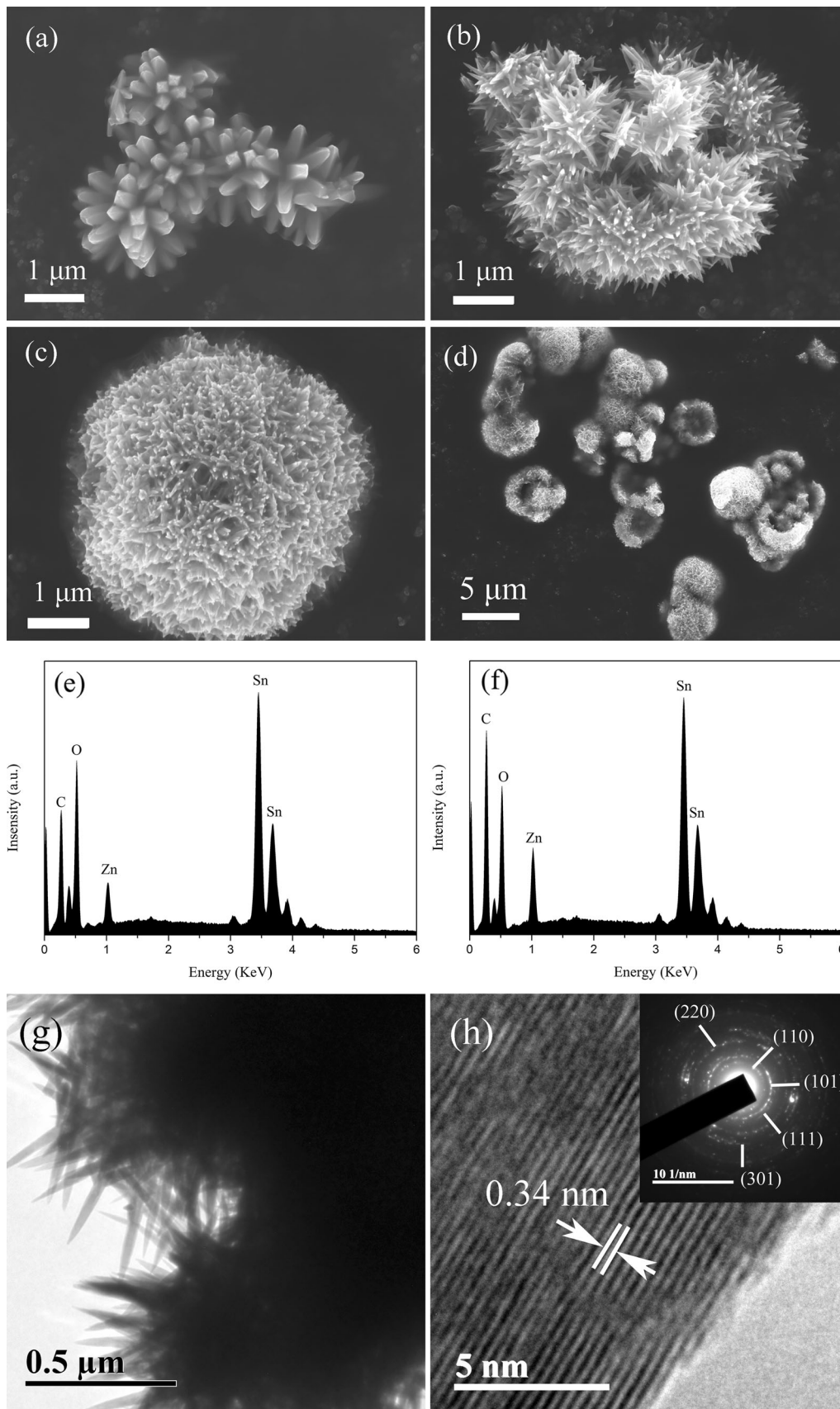


Fig. 3 SEM images of the as-prepared products: (a) undoped SnO₂, (b) 10 mol% Zn-doped SnO₂, and (c-d) 20 mol% Zn-doped SnO₂ in different magnifications. EDX patterns of (e) 10 mol% Zn-doped SnO₂ and (f) 20 mol% Zn-doped SnO₂. (g) TEM, (h) HRTEM, and SAED pattern (inset) images of 20 mol% Zn-doped SnO₂

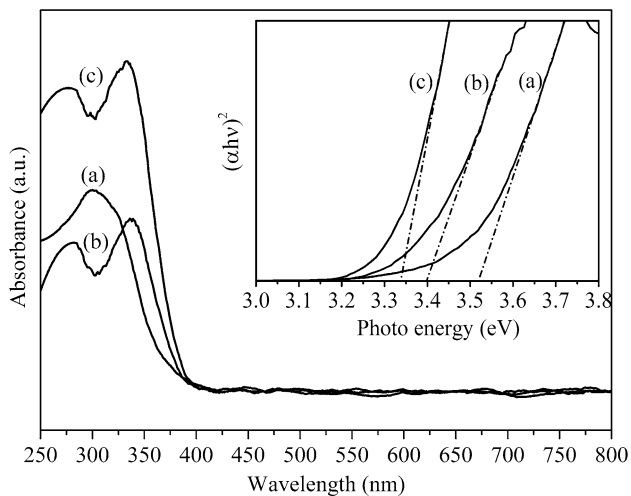


Fig. 4 UV-vis absorption spectra of the as-prepared products: (a) undoped SnO₂, (b) 10 mol% Zn-doped SnO₂, and (c) 20 mol% Zn-doped SnO₂

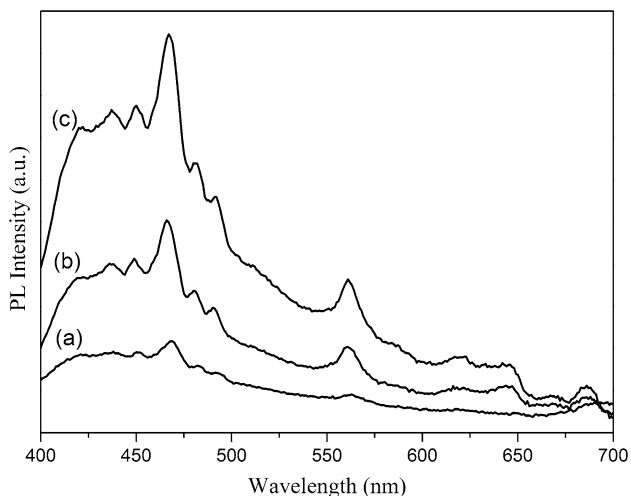


Fig. 5 PL spectra of the as-prepared products: (a) undoped SnO₂, (b) 10 mol% Zn-doped SnO₂, and (c) 20 mol% Zn-doped SnO₂

PL intensity is enhanced significantly with increasing Zn concentration. Since the band gap of the present products is 3.34–3.52 eV as determined from the UV-Vis absorption spectra, the observed visible luminescence bands cannot be ascribed to the direct recombination of a conduction electron in the Sn 4d band with a hole in the O 2p valence band. Generally, the bands observed in the visible region are related to defect energy levels originating from oxygen vacancies in the band gap of the SnO₂ nanoparticles. Zhang et al. (Ref 29) observed that Zn doping will introduce oxygen and Sn vacancies. Oxygen and Sn vacancy defects are easily formed at the nearest distance from the doped Zn atom. The formation energy for oxygen or Sn vacancy becomes smaller compared to that without Zn atom doping. Singh et al. (Ref 30) found that it becomes easier to form O (Sn) vacancy with the increasing Zn doping level. These studies indicate that doping Zn atoms in the SnO₂ system are beneficial to form oxygen and Sn vacancies. Furthermore, the Zn doping atoms preferentially sit on an interstitial site and act as a donor defect, donating one electron

to the system (Ref 31). It is indicated that upon donor doping, negative charges are introduced by the replacement of Sn with Zn in the SnO₂ lattice. Subsequently, oxygen vacancy center can trap the electron, leading to the formation of a Vo⁺ (Ref 32). The hole in the valence band can recombine with an electron in a deep trap Vo⁺ center to form the Vo⁺⁺ center, which suggested that the density of Vo⁺⁺ states would be high in the doped SnO₂. The recombination of electrons in the conduction band and holes in the Vo⁺⁺ states can be seen as visible emissions in the PL spectra (Ref 33).

The photocatalytic degradation of RhB under UV irradiation was used to evaluate the photocatalytic performance of undoped, 10 mol% Zn-doped, and 20% Zn-doped SnO₂, as shown in Fig. 6(a). It is observed that the concentration of RhB is hardly reduced under UV light irradiation in the absence of the photocatalyst. When Zn atoms are introduced into SnO₂, the degradation rate is increased to 67% for 10 mol% Zn-doped SnO₂ and reaches a maximum value of 83% for 20 mol% Zn-doped SnO₂ after 60-min irradiation. For a better comparison of the photocatalytic efficiency of different photocatalysts, kinetic analysis of degradation and mineralization of RhB in water was employed. The kinetic linear simulation curves of RhB photocatalytic degradation over different photocatalysts demonstrate that the above degradation reactions follow a Langmuir-Hinshelwood apparent first-order kinetics model due to the low initial concentrations of the reactants (Ref 34). The explanation is described below:

$$\ln(C/C_0) = k_{app}t,$$

where k_{app} is the apparent first-order rate constant (min⁻¹). The determined k_{app} values for different catalysts are summarized in Fig. 6(b). The photocatalytic efficiency order is 20 mol% Zn-doped SnO₂ > 10 mol% Zn-doped SnO₂ > undoped SnO₂, which is well consistent with the activity studies above.

The photocatalytic reaction in contact with Zn-doped SnO₂ surface is demonstrated as shown in Fig. 7. When light with energy higher or equal to the band gap energy is irradiated to the Zn-doped SnO₂ nanoparticles' surface, a photo-excited valence band electron is promoted to the conduction band, leaving behind a hole in the valence band, thus creating electron-hole pairs. The photo generated electrons and holes react with adsorbed surface substances, like O₂ and OH⁻, and form reactive species O₂^{•-} and OH* (hydroxyl radicals), respectively. These are the major oxidative species for the decomposition of organic pollutants. Oxidative species degrade the organic dye (RhB) into small molecules like CO₂, H₂O, NO₃⁻, and NH₄⁺ (Ref 3, 35). However, the photocatalytic activities of SnO₂ photocatalysts are usually limited by the fast recombination of the photogenerated electron-hole pairs (Ref 7, 8). It has been identified in the PL spectra that the density of Vo⁺⁺ states is high in the band gap for the 20 mol% Zn-doped SnO₂. These Vo⁺⁺ states act as a trap to capture the photoinduced electrons during the photocatalytic reactions (Ref 36–38). Consequently, undesirable recombination of photoinduced electron-hole pairs is effectively prevented, which may be the main reason for the enhanced photocatalytic activity.

Another factor contributing to the enhanced photocatalytic activity of 20 mol% Zn-doped SnO₂ is its hierarchical porous structure which is made up of small nanorods with high specific surface area. The reactant adsorption and photo-excitation are considered as the two most important steps in photocatalysis process. Based on SEM analysis, 20 mol% Zn-doped SnO₂ possesses the high specific surface area, which can provide

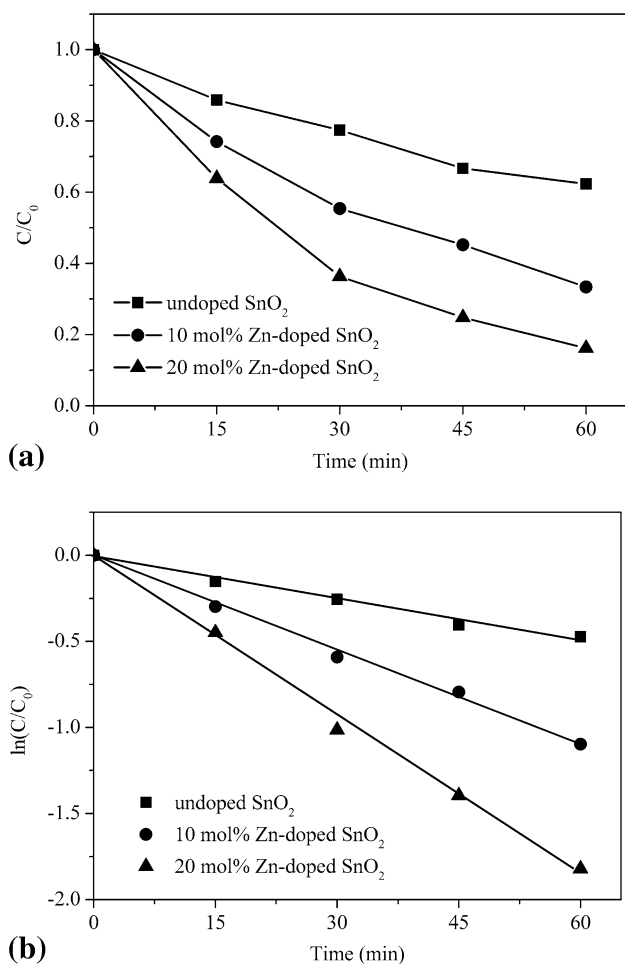


Fig. 6 (a) Photocatalytic degradation rate of RhB under UV light irradiation; (b) first-order linear plot of $\ln(C/C_0)$ versus the irradiation time of RhB degradation kinetics

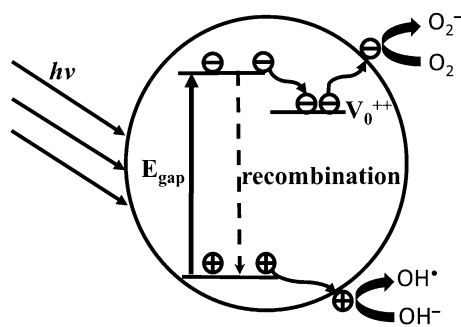


Fig. 7 The schematic diagram of photocatalytic degradation in the Zn-doped SnO_2 nanocrystals under the UV irradiation

more surface sites where the reactant molecules are adsorbed and then decompose via the redox reaction. Moreover, combined with UV-Vis absorption spectra, 20 mol% Zn-doped SnO_2 has high light harvesting ability, which enhanced utilization of excitation UV light. Thus the collective effects of the increased surface area and the unique hierarchical porous architecture induce better photocatalytic performance for 20 mol% Zn-doped SnO_2 compared with undoped and 10 mol% Zn-doped SnO_2 .

4. Conclusions

The undoped and Zn-doped SnO_2 products have been synthesized by a solvothermal method. Structural analysis revealed that the Zn-doped SnO_2 were highly crystalline with rutile structure, and no other secondary phase was found, which shows that the doped Zn^{2+} atoms were substituted in the Sn^{4+} sites. When increasing the Zn doping concentration from 0 to 20 mol%, the SnO_2 morphologies evolved from aggregated nanoprisms into hierarchically porous architecture assembled by nanorods with high aspect ratio (length/diameter), which indicated that the Zn incorporated in the crystal lattice influenced the anisotropic growth of SnO_2 . Based on the optical studies, it could be concluded that the substitutional doping of Zn influenced not only electronic structural modifications but also oxygen vacancies. The results of photocatalytic experiments showed that 20 mol% Zn-doped SnO_2 hierarchical spheres exhibited excellent efficiency of photocatalytic activity, which could be ascribed to their abundant oxygen vacancies, large specific surface area, and porous structure.

Acknowledgments

This work was supported by the National Natural Science Foundation of China (51172187, 51277138, 51402230, 61405151), SPDRF (20116102130002), 111 Program of MOE (B08040), the Natural Science Foundation of Shaanxi Province (Nos. 2014JQ8337, 2013KW12-02), the Scientific Research Program of Shaanxi Education Department (Nos. 15JK1325, 15JK1578), the Doctorate Foundation (BS1436) of China, the SKLP Foundation (KP201421), and the Fundamental Research Funds for the Central Universities (3102014JGY01004) of China.

References

1. C. Chen, W. Ma, and J. Zhao, Semiconductor-Mediated Photodegradation of Pollutants Under Visible-Light Irradiation, *Chem. Soc. Rev.*, 2010, **39**, p 4206–4219
2. L. Zheng, Y. Zheng, C. Chen, Y. Zhan, X. Lin, Q. Zheng, K. Wei, and J. Zhu, Network Structured SnO_2/ZnO Heterojunction Nanocatalyst with High Photocatalytic Activity, *Inorg. Chem.*, 2009, **48**, p 1819–1825
3. T. Lv, L. Pan, X. Liu, T. Lu, G. Zhu, and Z. Sun, Enhanced Photocatalytic Degradation of Methylene Blue by ZnO-Reduced Graphene Oxide Composite Synthesized via Microwave-Assisted Reaction, *J. Alloy. Compd.*, 2011, **509**, p 10086–10091
4. A. Bhattacharjee and M. Ahmaruzzaman, A Green and Novel Approach for the Synthesis of SnO_2 Nanoparticles and Its Exploitation as a Catalyst in the Degradation of Methylene Blue Under Solar Radiation, *Mater. Lett.*, 2015, **145**, p 74–78
5. Z. Chen, D. Pan, Z. Li, Z. Jiao, M. Wu, C. Shek, C.M.L. Wu, and J.K.L. Lai, Recent Advances in Tin Dioxide Materials: Some Developments in Thin Films, Nanowires, and Nanorods, *Chem. Rev.*, 2014, **114**, p 7442–7486
6. R. Yang, Y.G. Gu, Y.Q. Li, J. Zheng, and X.J. Li, Self-assembled 3-D Flower-Shaped SnO_2 Nanostructures with Improved Electrochemical Performance for Lithium Storage, *Acta Mater.*, 2010, **58**, p 866–874
7. W.W. Wang, Y.J. Zhu, and L.X. Yang, ZnO- SnO_2 Hollow Spheres and Hierarchical Nanosheets: Hydrothermal Preparation, Formation Mechanism, and Photocatalytic Properties, *Adv. Funct. Mater.*, 2007, **17**, p 59–64
8. Z. Liu, D.D. Sun, P. Guo, and J.O. Leckie, An Efficient Bicomponent $\text{TiO}_2/\text{SnO}_2$ Nanofiber Photocatalyst Fabricated by Electrospinning with a Side-By-Side Dual Spinneret Method, *Nano Lett.*, 2006, **7**, p 1081–1085

9. J. Schneider, M. Matsuoka, M. Takeuchi, J. Zhang, Y. Horiuchi, M. Anpo, and D.W. Bahnemann, Understanding TiO₂ Photocatalysis: Mechanisms and Materials, *Chem. Rev.*, 2014, **114**, p 9919–9986
10. X. Jia, Y. Liu, X. Wu, and Z. Zhang, A Low Temperature Situ Precipitation Route to Designing Zn-Doped SnO₂ Photocatalyst with Enhanced Photocatalytic Performance, *Appl. Surf. Sci.*, 2014, **311**, p 609–613
11. L.R. Hou, L. Lian, L. Zhou, L.H. Zhang, and C.Z. Yuan, Interfacial Hydrothermal Synthesis of SnO₂ Nanorods Towards Photocatalytic Degradation of Methyl Orange, *Mater. Res. Bull.*, 2014, **60**, p 1–4
12. S. Dai and Z. Yao, Synthesis of Flower-Like SnO₂ Single Crystals and Its Enhanced Photocatalytic Activity, *Appl. Surf. Sci.*, 2012, **258**, p 5703–5706
13. H. Zhang and C. Hu, Effective Solar Absorption and Radial Microchannels of SnO₂ Hierarchical Structure for High Photocatalytic Activity, *Catal. Commun.*, 2011, **14**, p 32–36
14. Y. Tang, P. Wee, Y. Lai, X. Wang, D. Gong, P.D. Kanhere, T. Lim, Z. Dong, and Z. Chen, Hierarchical TiO₂ Nanoflakes and Nanoparticles Hybrid Structure for Improved Photocatalytic Activity, *J. Phys. Chem. C*, 2012, **116**, p 2772–2780
15. H. Wang and A.L. Rogach, Hierarchical SnO₂ Nanostructures: Recent Advances in Design, Synthesis, and Applications, *Chem. Mater.*, 2013, **45**, p 123–133
16. A. Enesca, L. Andronic, and Anca Duta, Optimization of Optoelectrical and Photocatalytic Properties of SnO₂ Thin Films Using Zn²⁺ and W⁶⁺ Dopant Ions, *Catal. Lett.*, 2012, **142**, p 224–230
17. A.L. Patterson, The Scherrer Formula for X-ray Particle Size Determination, *Phys. Rev.*, 1939, **56**, p 978–982
18. W. Zhou, R. Liu, Q. Wan, Q. Zhang, A.L. Pan, L. Guo, and B. Zou, Bound Exciton and Optical Properties of SnO₂ One-Dimensional Nanostructures, *J. Phys. Chem. C*, 2009, **113**, p 1719–1726
19. N. Wang, X. Cao, and L. Guo, Facile One-Pot Solution Phase Synthesis of SnO₂ Nanotubes, *J. Phys. Chem. C*, 2008, **112**, p 12616–12622
20. P. Merle, J. Pascual, J. Camassel, and H. Mathieu, Uniaxial-Stress Dependence of the First-Order Raman Spectrum of Rutile. I. Experiments, *Phys. Rev. B.*, 1980, **21**, p 1617–1626
21. L.Z. Liu, X.L. Wu, F. Gao, J.C. Shen, T.H. Li, and P.K. Chu, Determination of Surface Oxygen Vacancy Position in SnO₂ Nanocrystals by Raman Spectroscopy, *Solid State Commun.*, 2011, **151**, p 811–814
22. A. Bouaine, N. Brihi, G. Schmerber, C. Ulhaq-Bouillet, S. Colis, and A. Dinia, Structural, Optical, and Magnetic Properties of Co-Doped SnO₂ Powders Synthesized by the Coprecipitation Technique, *J. Phys. Chem. C*, 2007, **111**, p 2924–2928
23. N. Mazumder, D. Sen, S. Saha, U.K. Ghorai, N.S. Das, and K.K. Chattopadhyay, Enhanced Ultraviolet Emission from Mg Doped SnO₂ Nanocrystals at Room Temperature and Its Modulation Upon H₂ Annealing, *J. Phys. Chem. C*, 2013, **117**, p 6454–6461
24. K. Vijayarangamuthu and S. Rath, Nanoparticle Nanopowders Size, Oxidation State, and Sensing Response of Tin Oxide Using Raman Spectroscopy, *J. Alloy. Compd.*, 2014, **670**, p 706–772
25. J.K. Jian, X.L. Chen, T. Xu, Y.P. Xu, L. Dai, and M. He, Synthesis, Morphologies and Raman-Scattering Spectra of Crystalline Stannic Oxide Nanowires, *Appl. Phys. A*, 2002, **75**, p 695–697
26. E.R. Leite, T.R. Giraldo, F.M. Pontes, and E. Longo, Crystal Growth in Colloidal Tin Oxide Nanocrystals Induced by Coalescence at Room Temperature, *Appl. Phys. Lett.*, 2003, **83**, p 1566–1568
27. Z. Zheng, B. Huang, X. Qin, X. Zhang, and Y. Dais, Strategic Synthesis of Hierarchical TiO₂ Microspheres with Enhanced Photocatalytic Activity, *Chem. Eur. J.*, 2010, **16**, p 11266–11270
28. Q.R. Zhao, Z.G. Zhang, T. Dong, and Y. Xie, Facile Synthesis and Catalytic Property of Porous Tin Dioxide Nanostructures, *J. Phys. Chem. B*, 2006, **110**, p 15152–15156
29. Y.L. Zhang, X.M. Tao, and M.Q. Tan, Origin of Ferromagnetism in Zn-Doped SnO₂ from First-Principles Study, *J. Magn. Magn. Mater.*, 2013, **325**, p 7–12
30. A.K. Singh, A. Janotti, M. Schewer, and C.G.V. Walle, Sources of Electrical Conductivity in SnO₂, *Phys. Rev. Lett.*, 2008, **101**, p 055502
31. S. Das and V. Jayaraman, SnO₂: A Comprehensive Review on Structures and Gas Sensors, *Prog. Mater. Sci.*, 2014, **66**, p 112–255
32. Y.C. Kim, C.H. Yoon, J. Park, J. Yoon, N.S. Han, J.K. Song, S.M. Park, and J.S. Ha, Effect of Sb Doping on the Optoelectronic Properties of SnO₂ Nanowires, *Thin Solid Films*, 2012, **520**, p 6471–6475
33. A. Kar, S. Kundu, and A. Patra, Surface Defect-Related Luminescence Properties of SnO₂ Nanorods and Nanoparticles, *J. Phys. Chem. C*, 2011, **115**, p 118–124
34. C. Wang, C. Shao, Y. Liu, and X. Li, Water-Dichloromethane Interface Controlled Synthesis of Hierarchical Rutile TiO₂ Superstructures and Their Photocatalytic Properties, *Inorg. Chem.*, 2009, **48**, p 1105–1113
35. S.K. Kansal, M. Singh, and D. Sud, Studies on Photodegradation of Two Commercial Dyes in Aqueous Phase Using Different Photocatalysts, *J. Hazard. Mater.*, 2007, **141**, p 581–590
36. J.C. Wang, P. Liu, X.Z. Fu, Z.H. Li, W. Han, and X.X. Wang, Relationship Between Oxygen Defects and the Photocatalytic Property of ZnO Nanocrystals in Nafion Membranes, *Langmuir*, 2008, **25**, p 1218–1223
37. J.Y. Shi, H.N. Cui, Z.B. Liang, X.H. Lu, Y.X. Tong, C.Y. Su, and H. Liu, The Roles of Defect States in Photoelectric and Photocatalytic Processes for Zn_xCd_{1-x}S, *Energy Environ. Sci.*, 2011, **4**, p 466
38. F. Xu, Y. Shen, L. Sun, H. Zeng, and Y. Lu, Enhanced Photocatalytic Activity of Hierarchical ZnO Nanoplate-Nanowire Architecture as Environmentally Safe and Facilely Recyclable Photocatalyst, *Nanoscale*, 2011, **3**, p 5020–5025